New calculation of the atmospheric neutrino flux in a three-dimensional scheme

M. Honda* and T. Kajita†
Institute for Cosmic Ray Research, University of Tokyo, Kashiwa-no-Ha, Chiba 277-8582, Japan

K. Kasahara‡
Shibaura Institute of Technology, Fukasaku, Ohmiya, Saitama 330-8570, Japan

S. Midorikawa§
Faculty of Engineering, Aomori University, Aomori 030-0943, Japan
(Received 22 April 2004; published 26 August 2004)

We have revised the calculation of the flux of atmospheric neutrinos based on a three-dimensional scheme with the realistic IGRF geomagnetic model. The primary flux model has been revised, based on the AMS and BESS observations, and the interaction model updated to DPMJET-III. With a fast simulation code and computer system, the statistical errors in the Monte Carlo study are negligible. We estimate the total uncertainty of the atmospheric neutrino flux prediction is reduced to $\lesssim 10\,\%$ below 10 GeV. The ''three-dimensional effects'' are found to be almost the same as the study with the dipole magnetic field, but the muon-curvature effect remains up to a few tens of GeV for horizontal directions. The uncertainty of the absolute normalization of the atmospheric neutrino is still large, above 10 GeV, due to the uncertainty of the primary cosmic ray flux above 100 GeV. However, the zenith angle variation is not affected by these uncertainties.

DOI: 10.1103/PhysRevD.70.043008 PACS number(s): 95.85.Ry, 14.60.Pq, 96.40.Tv

I. INTRODUCTION

The discovery of the neutrino oscillation from the study of atmospheric neutrinos is a one of the most important results in recent physical research [1] (see also Refs. [2–5], and Ref. [6] for a review). The study is carried out by the comparison of theoretical calculation of the atmospheric neutrino flux and experimental data. Therefore, it is desirable that both theoretical and experimental studies are improved. The SuperKamiokande is improving the statistics and the accuracy steadily for experimental data. It is important to improve the theoretical prediction of the atmospheric neutrino flux also.

There have been some improvements in the theoretical prediction of the atmospheric neutrino flux [7–12] (see Ref. [13] for a review). These studies were useful to determine the flux ratios between different types of neutrinos and the variation over zenith angle with good accuracy, and to establish neutrino oscillations and the existence of neutrino masses. We now wish to improve the accuracy of the absolute normalization as well as the ratio and directionality of the atmospheric neutrino fluxes for further studies.

In the time since our last comprehensive study of the atmospheric neutrino flux [7], knowledge of the primary cosmic ray has been improved by observations, such as BESS [15] and AMS [14] below 100 GeV. There have also been theoretical developments in hadronic interaction models, such as Fritiof 7.02 [16], FLUKA97 [17], and DPMJET-III [18]. Here, we adopt these revised primary flux and hadronic interaction models.

It has also been pointed out that the atmospheric neutrino flux calculated in a three-dimensional scheme is significantly different from that calculated in a one-dimensional scheme, at low energies for near-horizontal directions [9,19–24]. The one-dimensional approximation has been widely used in the past, and was used in our previous calculation and others [7,8]. This approximation is justified by the nature of hadronic interactions for calculations of high-energy ($\gtrsim 10$ GeV) atmospheric neutrino fluxes, but not at lower energies. With the computer resources then available, however, it was difficult to complete the calculation of atmospheric neutrino fluxes in a full three-dimensional scheme within a tolerable length of time. Some three-dimensional (3D) calculations employ approximations based on symmetry to circumvent the impact of limited computer resources. In Ref. [9], spherical symmetry is assumed, ignoring the magnetic field in the atmosphere, and in our previous three-dimensional calculation [21], we assumed an axial symmetry and used a dipole geomagnetic field model. Thus, a detailed calculation in a full three-dimensional scheme without symmetry remains a challenging job.

We have developed a new and fast simulation code for the propagation of cosmic rays in the atmosphere to calculate the atmospheric neutrino flux in a full three-dimensional scheme without having to assume symmetry. This fast simulation code and a fast computation system allow us to calculate the atmospheric neutrino flux with good accuracy over a wide energy region from 0.1 to a few tens of GeV, as is shown in this paper. The differences between three- and one-dimensional calculation schemes are similar to that we found in the study with a dipole geomagnetic field [21], and are small above a few GeV. The neutrino flux calculated in the three-dimensional scheme is smoothly connected to the one

*Electronic address: mhonda@icrr.u-tokyo.ac.jp; http://icrr.u-tokyo.ac.jp/~mhonda
†Electronic address: kajita@icrr.u-tokyo.ac.jp
‡Electronic address: kasahara@sic.shibaura-it.ac.jp
§Electronic address: midori@aomori-u.ac.jp

TABLE I. Parameters for all five components in the fit of Eq. (1).

parameter/component	α	K	b	c
Hydrogen (A=1)	2.74±0.01	14900±600	2.15	0.21
He (A=4)	2.64±0.01	600±30	1.25	0.14
CNO (A=14)	2.60±0.07	33.2±5	0.97	0.01
Mg–Si (A=25)	2.79±0.08	34.2±6	2.14	0.01
Iron (A=56)	2.68±0.01	4.45±0.50	3.07	0.41

calculated in the one-dimensional scheme at a few tens of GeV. We are therefore able to discuss the atmospheric neutrino flux up to 10 TeV in this paper.

Although progress in our theoretical study of the atmospheric neutrinos flux has been reported partly elsewhere [11,12], this is the first comprehensive report since 1995 [7].

II. PRIMARY COSMIC RAY FLUX MODEL

The primary flux model we use is based on the one presented in Refs. [25] and [13], in which the primary cosmic ray data below ~100 GeV are compiled and parametrized with the fitting formula

$$\phi(E_k) = K \times (E_k + b \exp[-c\sqrt{E_k}])^{-\alpha}, \quad (1)$$

where α, k, b, c are the fitting parameters. Although using the same fitting formula, the fitting parameters for nuclei heavier than helium are different in Refs. [25] and [13]. The parameters we used are taken from Ref. [13] and tabulated in Table I.

However, the extension of this flux model for cosmic ray protons does not agree with emulsion chamber experiments above ~10 TeV (the dashed line in Fig. 1). Therefore, we modified the power index above 100 GeV to −2.71, so that the fit passes through the center of the emulsion chamber experiments data (the solid line in Fig. 1). We also show the flux model for cosmic ray protons used in Ref. [7] as the dotted line in Fig. 1. Other than the cosmic ray protons, we use the same flux model as Ref. [13].

Note, we employ the superposition model for the cosmic ray nuclei, i.e., we consider a nucleus as the sum of individual nucleons, Z protons and $A-Z$ neutrons. The validity of the superposition model was discussed in Ref. [39] based on the Glauber formalism of nucleus–nucleus collisions [40]. The authors showed the interaction mean-free path of a nucleon in a nucleus is the same as a free nucleon and concluded that the superposition model is valid for the calculation of time averaged quantities, such as the fluxes of atmospheric neutrinos and muons. A similar discussion was also presented in Ref. [7] with the same conclusion.

III. HADRONIC INTERACTION

For the hadronic interaction model, we are using theoretically constructed models that have been successfully applied to detector simulations in high-energy accelerator experiments. In Ref. [7], we used NUCRIN [41] for 0.2 GeV

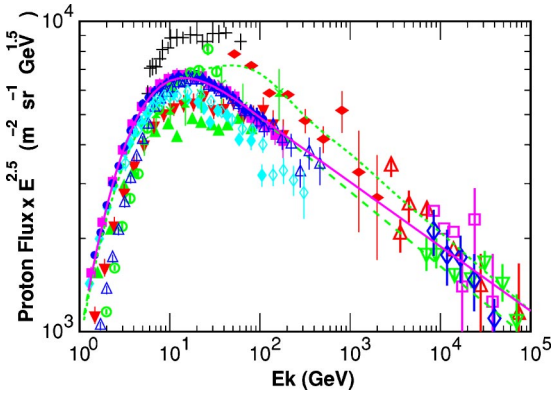

FIG. 1. (Color online) Primary cosmic ray observation and our model curves for protons at solar minimum. Crosses indicate data from Ref. [26], open circles indicate data from MASS [27], closed upward triangles LEAP [28], closed downward triangles IMAX [29], closed vertical diamonds CAPRICE-94 [30], open vertical diamonds CAPRICE-98 [31], closed circles BESS [15], closed horizontal diamonds AMS [14], open upward triangle BESS-TeV [32], closed horizontal diamonds Ryan *et al.* [33], open downward large triangles JACEE [34], open diamonds large RUNJOB [36,37], open upward large triangles from Ivanenko *et al.* [35], and open large squares from Kawamura *et al.* [38]. The dashed line shows the spectrum calculated with Eq. (1) and Table I, and the solid line shows that with the modification explained in the text. The dotted line is the proton flux model we used in Ref. [7].

$\leqslant E_{lab} \leqslant$ 5 GeV, FRITIOF version 1.6 [42] for 5 GeV $\leqslant E_{lab} \leqslant$ 500 GeV, and an original code developed by one of us [43] was used above 500 GeV. There were almost no improvements in the experimental study of the hadron interaction model of the multiple production, but there are noticeable improvements in the theoretical study, resulting in Fritiof 7.02 [16], FLUKA97 [17], and DPMJET-III [18].

To determine which is the better interaction model, we have used data on secondary cosmic ray muons [44–50] and gamma-rays [51] at balloon altitudes. The secondary cosmic rays at the balloon altitude are ideal for the study of the interaction model. They are approximately proportional to the air depth, and the ratio $[Flux/Depth]$ is determined almost only by the interaction and the flux of primary cosmic rays. On the other hand, the small statistics due to the small flux of secondary cosmic rays at balloon altitudes is the disadvantage for this study. The BESS 2001 flight is unique in this regard, as it measured the primary cosmic ray and muon fluxes simultaneously a little deeper in the atmosphere (4–30 g/cm^2) than normal long duration flights, and collected a sufficient number of muons and primary protons. In Fig. 2, we show the study made for muons observed by BESS 2001 [50]. Although it is hard to discriminate between other interaction models, it is found the DPMJET-III gives the best agreement between calculation and observation (for details, see Ref. [52]). Note that the momentum range shown in Fig. 2 is from 0.4 to 10 GeV/c. and that primary cosmic rays with energies from 6 to 80 GeV are mainly responsible for the muons in this momentum range at the balloon altitude [11,13]. Therefore, the study of the hadronic interaction model is for the primary cosmic rays in this energy region,

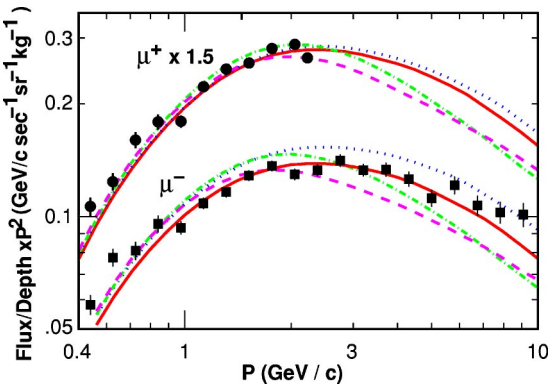

FIG. 2. (Color online) The quantity $[Flux/Depth]$ averaged over all the muon observation by BESS 2001 [52] at balloon altitudes. The lines are the same quantities calculated by DPMJET-III (solid line), Fritiof 1.6 (dashed line), Fritiof 7.02 (dotted line), and FLUKA 97 (dash-dot).

corresponding to the neutrinos of 0.3–4 GeV.

For the wider energy region of primary cosmic rays, we may examine the hadronic interaction model using the observed muons at different altitudes and at sites with different cutoff rigidities. Note that at ground level the muon fluxes are available for a wider momentum range with good statistics. We are preparing a paper [53] for such a study with the muon fluxes observed by BESS [54–56], and so limit ourselves here to comment that the muon flux observed by BESS is reproduced with DPMJET-III with an accuracy of ~ 5 % for the muons in the ''important'' momentum range from one to a few tens of GeV/c for most cases. At ground level, the primary cosmic rays with energies from 20 to a few 100 GeV are responsible for the muons in this momentum range, corresponding to neutrinos of 1–10 GeV. This study was partly reported in Ref. [11].

We do not use the original package of the hadronic interaction code in the calculation of atmospheric neutrino fluxes. We first carry out a computer experiment of the interaction of all kinds of primary or secondary cosmic rays with air-nuclei, using the original hadronic interaction code. Then, the ''data'' are used to construct an inclusive interaction code, which reproduces the multiplicities and energy spectra of secondary particles of the original code. The inclusive interaction code violates the conservation laws for energy-momentum and other quantum numbers in a single interaction, but they are restored statistically. Note that for the secondary particles whose lifetime is shorter than 10^{-9} sec we record their decay products as the data. The experiment scans the energy region from 0.2 to 10^6 GeV in kinetic energy, and is repeated typically 1 000 000 times for each kind of projectile and each injection energy.

For the energy distribution of secondary particles in the interaction, we fit the original distribution of x, defined as $x \equiv E_k^{sec}/E_k^{proj}$, with the combination of B-spline functions for each kind of projectile particle, each injection energy, and each kind of secondary. Then the inclusive code uses the B-spline-fit to reproduce the energy distribution of the secondary particle with a good accuracy. For the scattering angles, we calculate the average transverse momentum ($\langle p_\perp \rangle$) for each kind of projectile, each injection energy, each kind of secondary, and each secondary energy. In the inclusive code, we sample the scattering angle (θ) with the distribution function $\propto \exp(a \cdot \cos\theta) \cdot d\cos\theta$, where a is determined so that $\langle p_\perp \rangle$ is the same as the original interaction model. The $p_\perp$-distribution approaches $\propto \exp(-a' \cdot p_\perp^2) \cdot p_\perp dp_\perp$ and $a' = \pi/(2\langle p_| \rangle)^2$ for $p \gg 1$ GeV/c. Note, the inclusive code constructed for DPMJET-III reproduces not only $\langle p_\perp \rangle$ but also, approximately, the original $p_\perp$-distribution for $p_\perp < 1$ GeV/c. There is a longer tail in the original $p_\perp$ distribution for larger $p_\perp$. However, since the number of secondary particles that have $p_\perp > 1$ GeV/c is limited, they are not important in this study.

The constructed inclusive codes are typically ~ 100 times faster than the original package. The fast computation is very important in the three-dimensional calculation of the flux of atmospheric neutrinos, as well as the study of secondary cosmic rays. Note, however, the inclusive interaction code is only valid for the calculation of a time averaged quantity, such as the fluxes of atmospheric neutrinos and muons. The situation is similar to the superposition model for the nuclear cosmic rays.

IV. CALCULATION SCHEME

Except for the geomagnetic field model, the simulation scheme is similar to the previous three-dimensional calculation [21] in which we assumed a dipole geomagnetic field. In this calculation, we use the IGRF geomagnetic field model [57] with the tenth-order expansion of spherical functions for the year 2000. As the geomagnetic field changes very slowly, the neutrino flux calculated for the year 2004 would not show a noticeable difference. We use the US-standard 1976 [58] atmospheric model, as in the previous study. Note that for a study of the seasonal variations of atmospheric neutrino fluxes we need to use a more sophisticated and detailed atmospheric model [59].

We assume the surface of the Earth is a sphere with radius of $R_e = 6378.180$ km. We also assume three more spheres: the injection, simulation, and escape spheres. The radius of the injection sphere is taken as $R_{inj} = R_e + 100$ km, the simulation sphere as $R_{sim} = R_e + 3000$ km, and the escape sphere as $R_{esc} = 10 \times R_e$. The sizes of the injection sphere (R_{inj}) and escape sphere (R_{esc}) are the same as in the previous study [21].

The cosmic rays are sampled on the injection sphere uniformly toward inward directions, following the given primary cosmic ray spectra. Before they are fed to the simulation code for propagation in air, they are tested to determine whether they can pass the rigidity cutoff, i.e., the geomagnetic barrier. For a sampled cosmic ray, the ''history'' is examined by solving the equation of motion in the negative time direction. When the cosmic ray reaches the escape sphere without touching the injection sphere again in the inverse direction of time, the cosmic ray can pass through the magnetic barrier following the trajectory in the normal direction of time. In the one-dimensional calculation we normally prepare a cutoff table for each neutrino detector site beforehand, but it is practically impossible to construct such a table

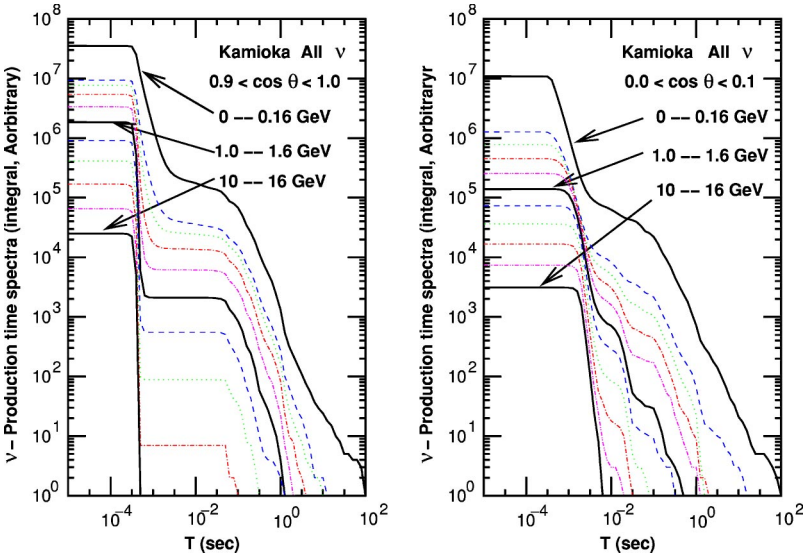

FIG. 3. (Color online) Integral production time distribution for the atmospheric neutrinos observed at Kamioka. For the neutrino energies, we divide each decade into five bins and show the production time spectra in solid, dashed, dash-dot, dash-dot-dot, and dash–3-dot lines.

for the three-dimensional calculation. Note, all the nucleons carried by the cosmic ray nuclei are treated as protons with double rigidity (= momentum for protons), before the first interaction with an air-nucleus and in the rigidity cutoff test.

The propagation of cosmic rays is simulated in the space between the surface of Earth and the simulation sphere. When a particle enters the Earth, it loses its energy very quickly, and generates neutrinos with energy less than 100 MeV only. Therefore, we discard such particles as soon as they enter the Earth, as most neutrino detectors that observe atmospheric neutrinos do not have sensitivity below 100 MeV.

For secondary particles produced in the interaction of a cosmic ray and air-nucleus, there is the possibility that they go out and re-enter the atmosphere and create neutrinos with energy ~ 1 GeV. Therefore, too small a simulation sphere may miss such secondary particles. On the other hand, it is very time consuming to follow all the particles out to distances far from the Earth. In the previous study, we took the radius of simulation sphere to be $R_{sim}=R_e+300$ km, and showed that this is sufficient to calculate the neutrino flux to within a accuracy of ~ 1 % from an analysis of the neutrino production time after the first interaction [60]. In this paper, however, we adopt a radius for the simulation sphere of $R_{sim}=R_e+3000$ km for greater accuracy, since we found the average computation time for a primary cosmic ray does not increase that rapidly up to a simulation sphere of this size. Regarding the size of simulation sphere, we study the neutrino production time after the injection of the primary cosmic ray in Sec. IV A.

We ''observe'' the neutrino at the surface of the Earth, and the size of the ''virtual detector'' is closely related to the accuracy of the calculated flux and computation time. With too large a virtual detector, the average observation conditions, such as the dependence on the geomagnetic field, may differ from the real site. However, with too small a virtual detector, it is difficult to collect a sufficient number of neutrinos within a reasonable computation time. In the previous study, we assumed an axial symmetry with dipole geomagnetic field, and considered a belt around the Earth as the virtual detector. For the more realistic geomagnetic field model IGRF, we consider a localized virtual detector, the surface of the Earth inside a circle with the radius of ~ 1117 km (center angle of 10°) around the target detector. The virtual detector is $\sim \frac{1}{6}$ the size of the previous one.

Note, we placed many virtual detectors on the Earth corresponding to the existing neutrino detectors, and recorded neutrinos for each detector at the same time. However, we only show the results for the virtual detectors placed at Kamioka and North America in this paper, as they are good examples of a low magnetic latitude and a high magnetic latitude, respectively. The fluxes for Soudan and Sudbury are almost identical, and we refer to them here as North America.

A. Neutrino production time

Before showing the resulting atmospheric neutrino flux, we would like to introduce some interesting quantities: the neutrino production time and the impact parameter of primary cosmic rays. These quantities provide important hints for the efficient calculation of atmospheric neutrino fluxes in the three-dimensional scheme.

First, we show the study of neutrino production time. Before the calculation of atmospheric neutrino fluxes, we studied the neutrino production time to optimize the size of simulation sphere. Note, the radius of the simulation sphere used in this study is $R_{sim}=10\times \mathrm{Re}=63\,781.80$ km, and so neutrinos produced within $t_{free}=2\times(R_{sim}-R_{inj})/c\sim 0.4$ sec after the injection of cosmic ray at the injection sphere are absolutely free from the boundary, by the naïve discussion of the causality.

We show the integral distribution of the neutrino production time for neutrinos observed in Kamioka in Fig. 3. The production time is measured after the injection of the cosmic ray at the injection sphere. We find that t_{free} for $R_{sim}=R_e+3000$ km (~ 20 msec) is large enough to calculate the flux of atmospheric neutrinos with an accuracy much better than 1 %. It is interesting that there is a second peak at ~ 0.1 sec due to the albedo particle reported by AMS.

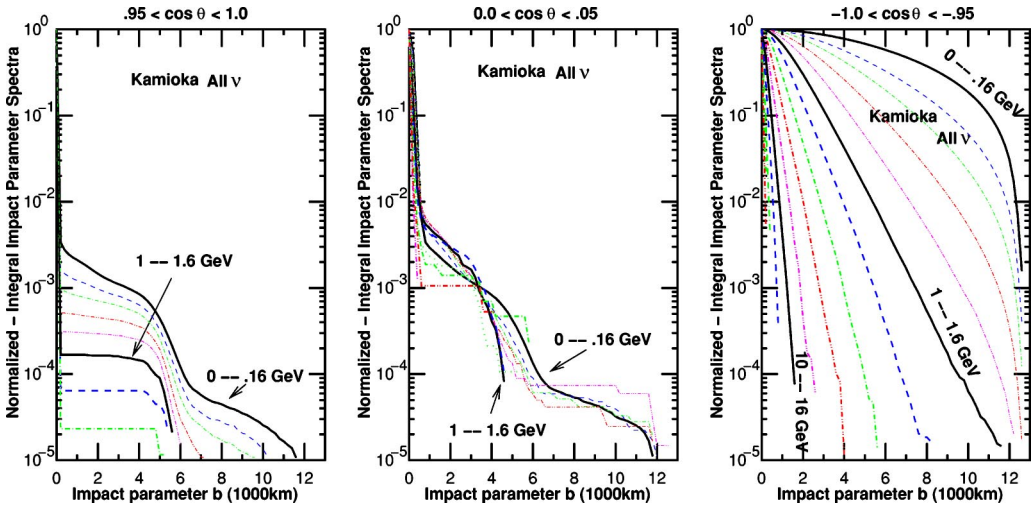

FIG. 4. (Color online) Normalized integral impact parameter distribution of the primary cosmic rays that produce neutrinos observed at Kamioka. Each decade of neutrino energy is divided into five bins, and the impact parameter spectra are shown by solid, dashed, dash-dot, dash-dot-dot, and dash−3-dot lines.

We used $R_{sim}=R_e+300$ km in the previous study [21], and reported that this R_{sim} is sufficient for calculation of atmospheric neutrino fluxes with an accuracy of ~ 1 % [60]. Note there is a ~ 0.3 msec time offset in the production time after the injection for vertical directions and a ~ 3 msec time offset for horizontal directions. Considering that the offset time is different for each injected cosmic ray, the study of the production time after the first interactions of cosmic rays requires a more sophisticated study than the present one. We can expect much better accuracy with $R_{sim}=R_e+3000$ km.

The same study has been carried out for other neutrino detector sites. However, the distributions are similar to that of Kamioka except for the height and position of the second peak. The second peak is lower and at larger production time for the higher latitude site.

B. Impact parameter of the primary cosmic rays

Here, we study the impact parameter of cosmic rays that produce a neutrino passing through the detector. When the cosmic ray produces a neutrino going through a virtual detector, the impact parameter (b) is calculated against the contact point of the neutrino and the surface of Earth for the input primary cosmic ray at the injection sphere.

The impact parameter distributions are normalized and integral form are shown for Kamioka in Fig. 4. As expected, the impact parameters of downward going neutrinos are distributed in a narrow region near $b=0$, while those of upward going neutrinos are widely distributed. However, we find the distribution shrinks to $b=0$ as the neutrino energy increases, and for neutrinos with energy >10 GeV, most neutrinos (>99 %) are produced by primary cosmic rays with b <1000 km.

The study of impact parameters can be used to accelerate the calculation of the atmospheric neutrino flux above $\gtrsim 10$ GeV. Selecting an impact parameter for primary cosmic rays of <2000 km at the injection results in atmospheric neutrino flux calculations ~ 30 times faster than the original calculation scheme explained above. We use this acceleration technique for the neutrino flux above 10 GeV.

In Kamioka, it is found that the impact parameter distribution has a structure at 5–6000 km for the vertical directions and 3–5000 km for horizontal directions. This is considered again to be the effect of the albedo particles observed by AMS [14]. However, the contribution is small ($\ll 1$ %). The same study has been done for other neutrino detector sites. However, the concentration of the impact parameter distribution to $b=0$ is quicker than Kamioka for downward going neutrinos, as they site at higher geomagnetic latitudes than Kamioka. For upward going neutrinos, the impact parameter distribution is almost the same for all the sites.

V. THE FLUX OF ATMOSPHERIC NEUTRINOS

Without limiting the impact parameter, we sampled 307 618 204 971 cosmic ray nucleons before the rigidity cutoff test and simulated the propagation in air for 116 086 900 000 nucleons with kinetic energy >1 GeV, or equivalently all the cosmic rays with $E_k/A>1$ GeV arrive on the injection sphere in 8.07×10^{-8} second. Limiting the impact parameter, we sampled 415 711 823 606 cosmic ray nucleons before the rigidity cutoff and impact parameter test and simulated the propagation in air for 25 413 045 195

TABLE II. Interaction and geomagnetic field models in the calculations.

Calculation	Int. Model	Geomagnetic Field (Rigidity cutoff)	Geomagnetic Field (In air)
3D	DPMJET-III	IGRF	IGRF
FLUKA [9]	FLUKA [a]	IGRF	None
DIPOLE [21]	Fritiof 1.6 base	Dipole	Dipole
1D	DPMJET-III	IGRF	none

[a]Advanced version from FLUKA97

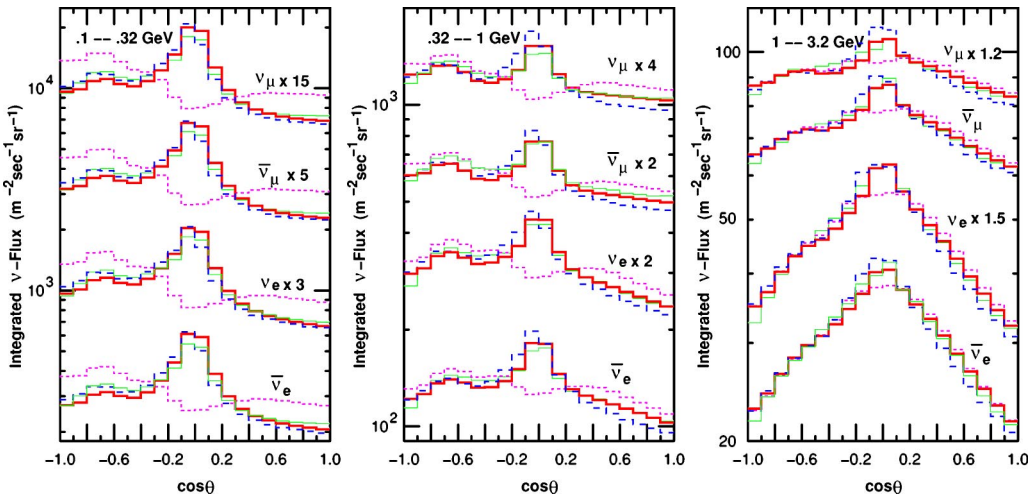

FIG. 5. (Color online) Zenith angle dependence of the atmospheric neutrino flux at Kamioka in three energy bins. For the azimuthal directions, averages are taken. The thick solid lines are for 3D, dotted lines for 1D, dashed lines for FLUKA, and thin solid lines for DIPOLE.

nucleons with kinetic energy >10 GeV or equivalently all the cosmic rays with $E_k/A>10$ GeV arrive on the injection sphere in 1.4 microsecond. Note the flux tables for Kamioka, Gran Sasso, and North America calculated in this study are available at http://www.icrr.u-tokyo.ac.jp/~mhonda .

In this section we present the characteristic features of the atmospheric neutrino flux calculated in the three-dimensional scheme (3D) and compare them with those calculated in the one-dimensional scheme with the same primary cosmic ray flux and interaction model. To study the differences due to the interaction model and the calculation scheme in three-dimensional calculation, we also compare the atmospheric neutrino flux calculated in Ref. [9] (FLUKA), and the one calculated in our previous three-dimensional study with the dipole magnetic field [21] (DIPOLE). Note, the interaction model used in DIPOLE is the same as Ref. [7]. Interaction models and the geomagnetic field models used in the calculations are summarized in Table II.

For Kamioka and Gran Sasso, we calculated the atmospheric neutrino fluxes considering the effect of the surface structure (mountains) above the neutrino detectors. However, in the following studies, we use the neutrino flux calculated for a flat detector at sea level, i.e., ignoring surface structure, to see the differences due to the calculation schemes.

A. Zenith angle dependence of the neutrino flux

The most prominent difference between three- and one-dimensional atmospheric neutrino flux calculations is the horizontal enhancement at low energies. (For the origin of the horizontal enhancement, see Refs. [13,19,21].) We compare the zenith angle dependences of atmospheric neutrino fluxes calculated in the 3D, 1D, FLUKA, and DIPOLE cases for Kamioka (Fig. 5) and North America (Fig. 6), integrating over several energy bins and averaging over azimuth angles.

In these figures, we see the horizontal enhancements in 0.1–0.32 GeV and 0.32–1 GeV energy bins for all the three-

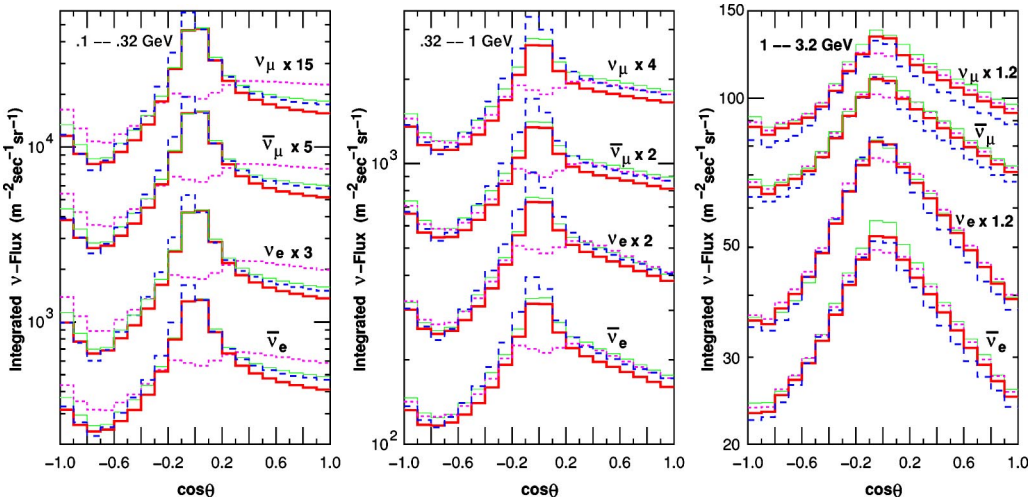

FIG. 6. (Color online) Zenith angle dependence of the atmospheric neutrino flux at North America in three energy bins. For the azimuthal directions, averages are taken. The notation for lines is the same as Fig. 5.

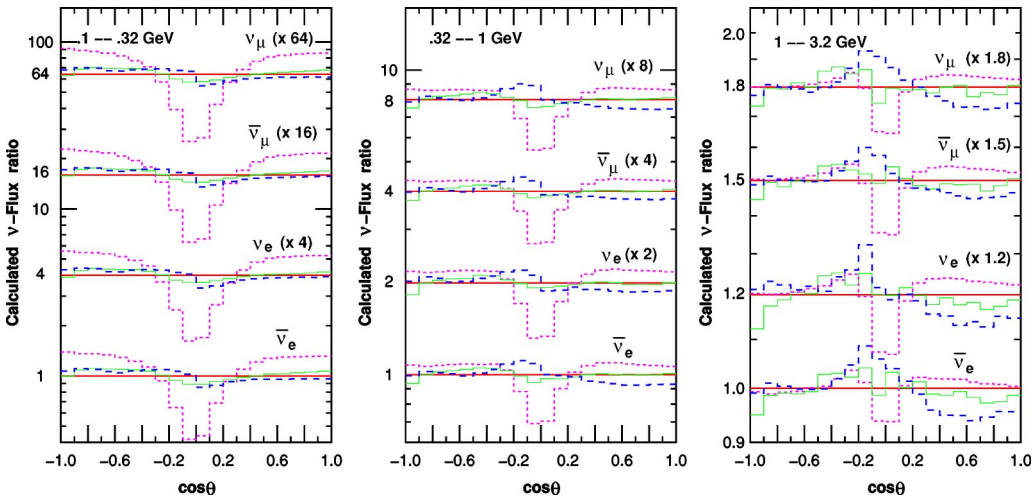

FIG. 7. (Color online) The normalized ratio of each flux to the 3D case as a function of zenith angle, for Kamioka. Dotted lines are for 1D, dashed lines for FLUKA, and thin solid lines for DIPOLE.

dimensional calculations. On the other hand, the flux near horizontal directions is rather smaller than neighboring directions in the 1D case due to the high cutoff rigidities. In the 1–3.2 GeV energy bin, the differences between the calculations are small. To study the difference of zenith angle dependencies of neutrino fluxes due to the calculation scheme, we normalize each flux by the omnidirectional flux average and depict the ratio to the 3D case in Figs. 7 and 8 as a function of zenith angle.

In these figures, we find that the horizontal enhancement still exists in the 1–3.2 GeV energy bin, but that it decreases rapidly with neutrino energy. The difference at near-horizontal directions is more than 50 % in 0.1–0.32 GeV bin, but it reduces to $\lesssim$10 % in 1–3.2 GeV bin, for all kinds of neutrino.

The differences among the three-dimensional calculations (3D, FLUKA, DIPOLE) are small, especially that between 3D and DIPOLE. However, the amplitude of the horizontal enhancement in DIPOLE is clearly slightly smaller than that in the 3D calculation. This is thought to be due to the difference of interaction model, especially to the average transverse momentum of secondary mesons. Note, the $\langle P_t \rangle$ of pions is 0.289 GeV/c in DPMJET-III, while it is 0.256 GeV/c in Fritiof 1.6 for **P** + Air interactions at $E_{lab}=10$ GeV. The difference between 3D and FLUKA is asymmetric below and above the horizontal direction ($\cos\theta=0$). It is difficult to deduce differences in the interaction model in this comparison.

To see the energy dependence of the horizontal enhancement more clearly, we compared the 3D and 1D energy spectra for vertical and horizontal directions averaging over azimuth angles in Figs. 9 (Kamioka) and 10 (North America). We find the differences disappear at $\sim$1 GeV for vertical directions, and $\sim$3 GeV for horizontal directions, for all neutrinos.

Moreover, we find the fluxes averaged over all directions for 3D and 1D cases are very close to each other, even at low

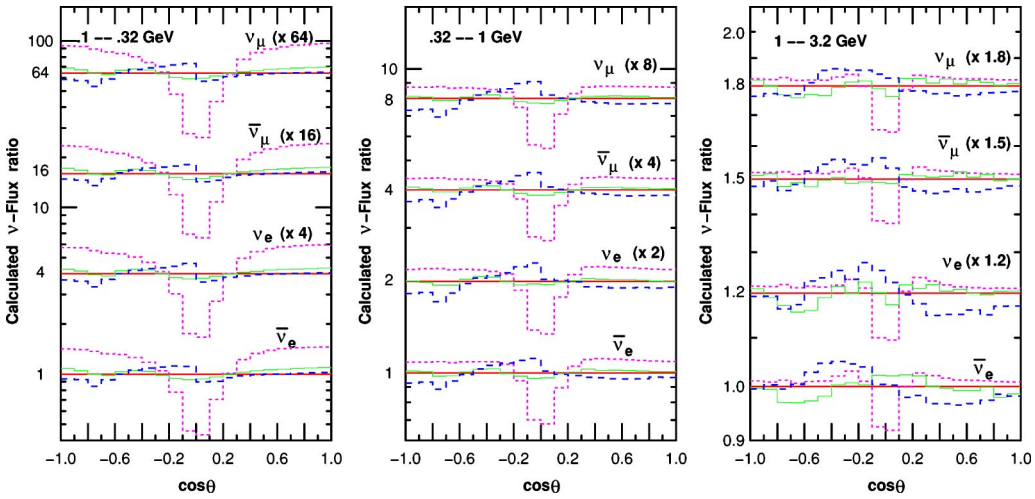

FIG. 8. (Color online) The ratio of atmospheric neutrino fluxes calculated by 1D, FLUKA, and DIPOLE for North America to that from the 3D case. The notations are the same as for Fig. 7.

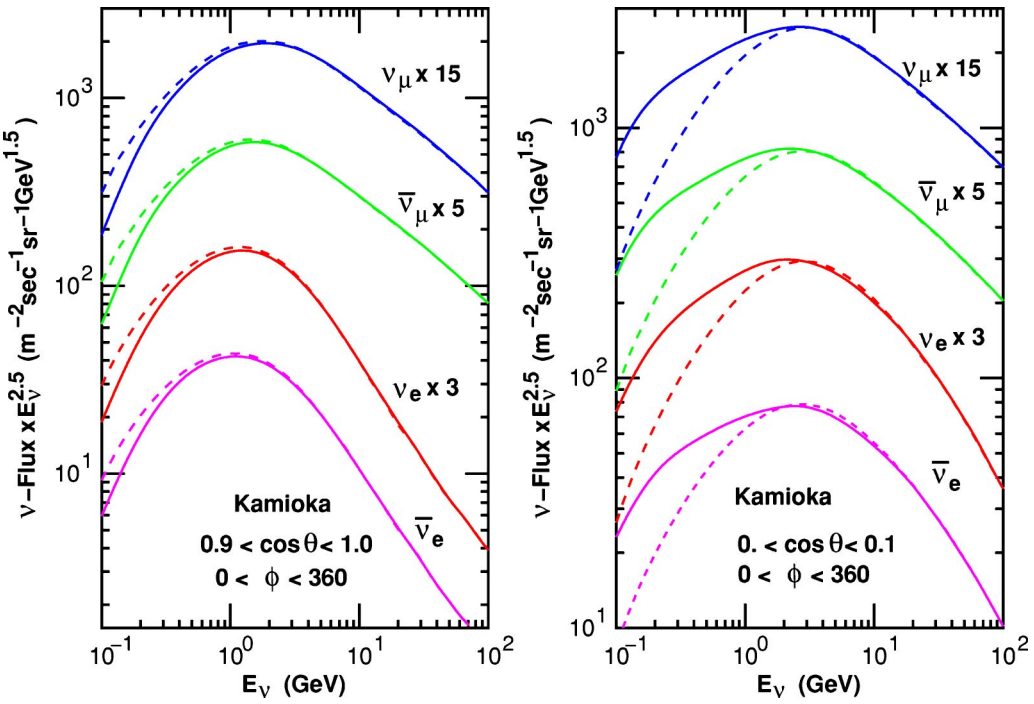

FIG. 9. (Color online) Atmospheric neutrino fluxes at Kamioka for 3D and 1D, averaged over azimuth angles. The left panel shows the comparison for vertical directions, and the right panel for horizontal directions. The solid lines show the 3D results and the dashed lines the 1D results.

energies. Averaging the neutrino fluxes in Figs. 5 and 6 over zenith angles, the 3D/1D ratios are tabulated in Table III. They agree with each other to within a few percent in all cases.

B. East–West effect

Here, we use the 3D and 1D fluxes only, since they are calculated under the same conditions (except for the one- or

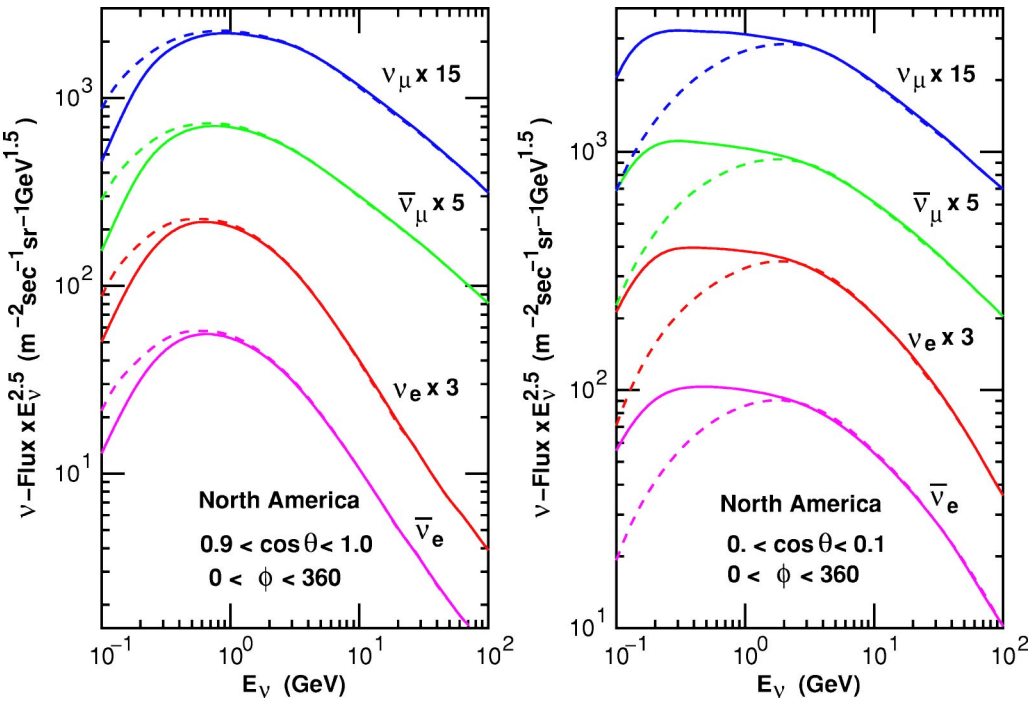

FIG. 10. (Color online) Atmospheric neutrino fluxes at North America for 3D and 1D, averaged over azimuth angles. The left panel shows the comparison for vertical directions, and the right panel for horizontal directions. The solid lines show the 3D results and the dashed lines the 1D results.

TABLE III. 3D/1D ratio for the all-direction average of atmospheric neutrino flux.

E_ν(GeV)	ν_μ	$\bar{\nu}_\mu$	ν_e	$\bar{\nu}_e$
		Kamioka		
0.1–.32	0.979	0.980	0.970	0.978
.32–1.0	0.997	1.000	0.999	0.992
1.0–3.2	0.983	0.984	0.982	0.975
		North America		
0.1–.32	1.036	1.035	1.028	1.025
.32–1.0	1.019	1.020	1.021	1.014
1.0–3.2	0.992	0.990	0.989	0.985

three-dimensional calculation scheme). Contrary to the quantitative agreements between 3D and 1D above, a few GeV in the azimuthally averaged fluxes, they are quite different when the azimuth angles are limited to East or West directions, even at higher energies ($\sim$10 GeV).

We depict the 3D and 1D atmospheric neutrino fluxes arriving horizontally ($0<\cos\theta<0.1$) from the East ($60°<\phi<120°$), and West ($240°<\phi<300°$) for Kamioka (Fig. 11) and North America (Fig. 12), where we measure the azimuth angle from South ($\phi=0$), and $\phi=90°$, 180°, and 270° are East, North, and West directions, respectively.

The differences in the fluxes from the 3D and 1D calculations for different kinds of neutrinos may be classified into two groups, ν_μ and $\bar{\nu}_e$, and $\bar{\nu}_\mu$ and ν_e. The former group are the decay products of μ^-, and the latter are the decay products of μ^+. The geomagnetic field deflects μ^+'s toward the same direction as for primary cosmic rays. Therefore, it enhances the East and West differences of the $\bar{\nu}_\mu$ and ν_e fluxes caused by the rigidity cutoff. On the other hand, the geomagnetic field works on the μ^-'s in the opposite direction to that for primary cosmic rays. Therefore, it reduces the East and West differences for the ν_μ and $\bar{\nu}_e$ fluxes caused by the rigidity cutoff [20]. In the Figs. 11 and 12, we mainly see the horizontal enhancement in the neutrino energies $\lesssim$1 GeV in the difference of 3D and 1D. For $\gtrsim$1 GeV, however, the muon curvature in the geomagnetic field is a larger effect than the horizontal enhancement, and this extends to several tens of GeV for near horizontal directions.

The muon curvature effect should be seen in the azimuthal variation of the atmospheric neutrino fluxes. We show the integrated azimuthal angle dependence in the same energy bins as in Sec. V A for Kamioka (Fig. 13) and North America (Fig. 14). Also we tabulated the ratio of maximum to minimum fluxes in the figures in Table IV, to see the variation amplitude. In the 1D case, the amplitudes are similar to each other for all kinds of neutrinos in each energy bin. This is because the 1D azimuthal variation is caused by the rigidity cutoff of the primary cosmic rays. In the 3D case, the amplitudes are different among the different kinds of neutrino even in the same energy bin. The amplitudes of ν_μ and $\bar{\nu}_e$ are suppressed, while those of $\bar{\nu}_\mu$ and ν_e are enhanced, except for the lowest energy bin of 0.1–0.32 GeV. In the lowest energy bins, smearing suppresses the 3D azimuth angle dependence.

Note that ν_e has the largest amplitude among all ν's in 3D. This is because about 1/2 of the $\bar{\nu}_\mu$'s are created by pion decay directly, while all the ν_e's are created by μ decay at

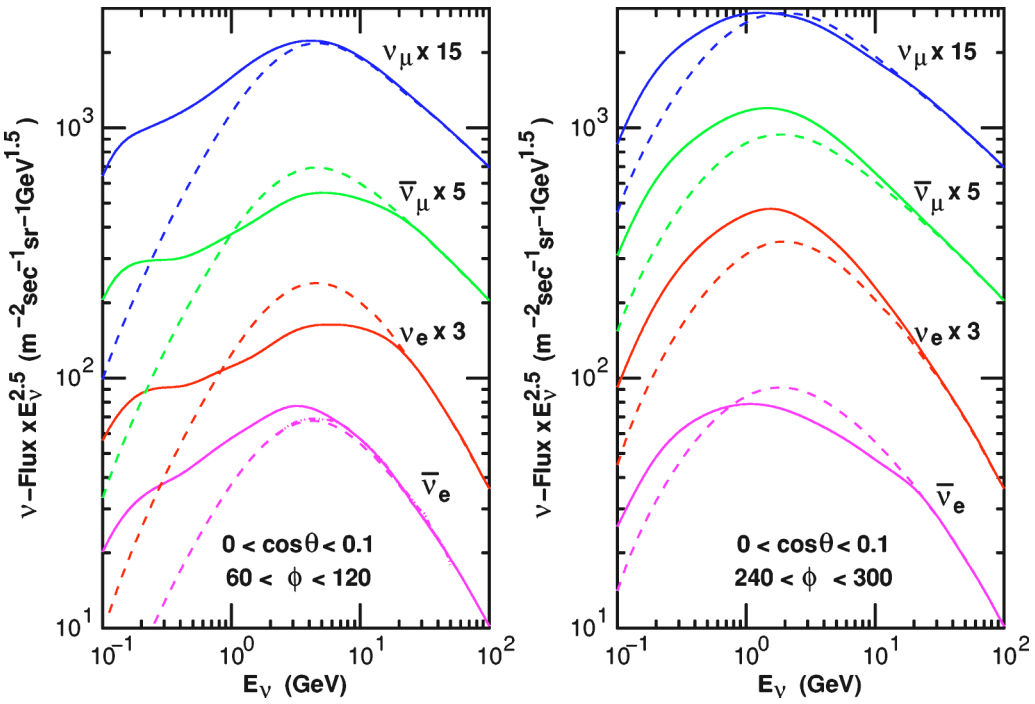

FIG. 11. (Color online) The flux of horizontal ($0<\cos\theta<0.1$) atmospheric neutrinos arriving from the East ($60°<\phi<120°$) (left), and West ($240°<\phi<300°$) (right) directions at Kamioka. The solid lines show the result of the 3D calculation and the dashed line the 1D case.

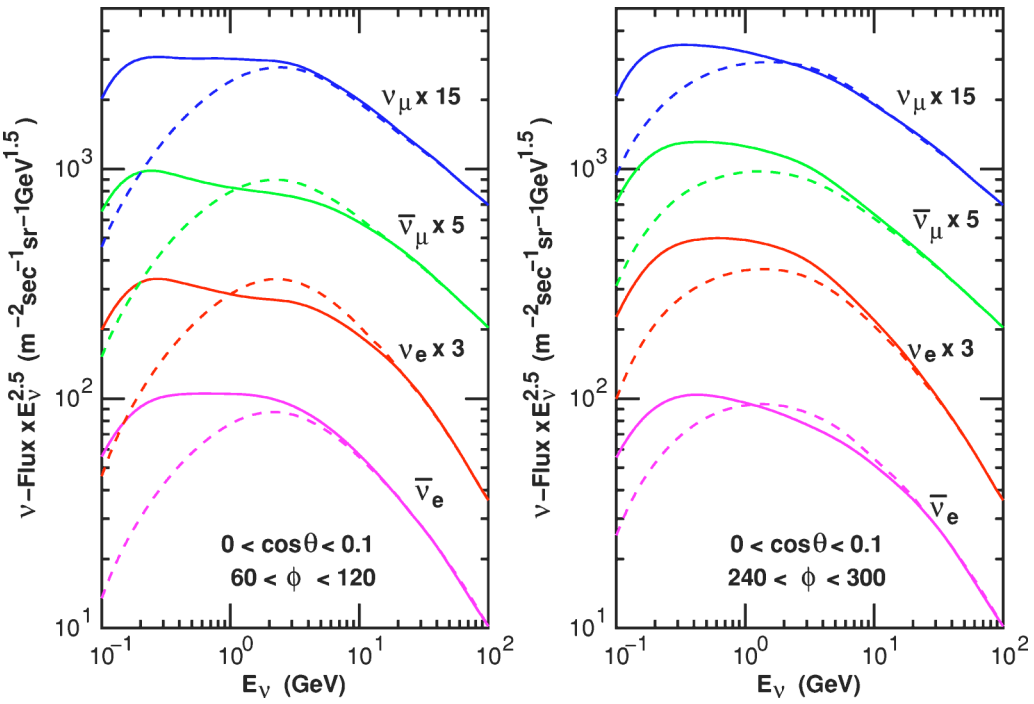

FIG. 12. (Color online) The flux of horizontal ($0<\cos\theta<0.1$) atmospheric neutrinos arriving from the East ($60°<\phi<120°$) (left), and West ($240°<\phi<300°$) (right) directions at North America. The solid lines show the result of the 3D calculation and the dashed line the 1D case.

these energies. It is noteworthy that the amplitude of ν_e in the 1–3.2 GeV energy bin is still large. This is important for the experimental confirmation of the effect of muon curvature, because the determination of the arrival direction is better for higher energy neutrinos.

Generally speaking, the azimuthal angle dependence of atmospheric neutrinos at high magnetic latitude sites, such as North America, is smaller than that at low magnetic latitude sites, such as Kamioka, because the rigidity cutoff is too low. However, we find in Fig. 14 and Table IV that the difference in the azimuthal angle dependence of atmospheric neutrinos between 3D and 1D due to the muon curvature is similar to that for the low magnetic latitude site.

VI. NEUTRINO FLUXES AT HIGHER ENERGIES

In this section, we study the atmospheric neutrino flux at higher energies than in Sec. V. First, we note that the atmospheric neutrino fluxes above 10 GeV have a much larger uncertainty than those below 10 GeV. The main reasons are the uncertainties in the primary cosmic rays and the hadronic interaction model at energies above 100 GeV. As the differ-

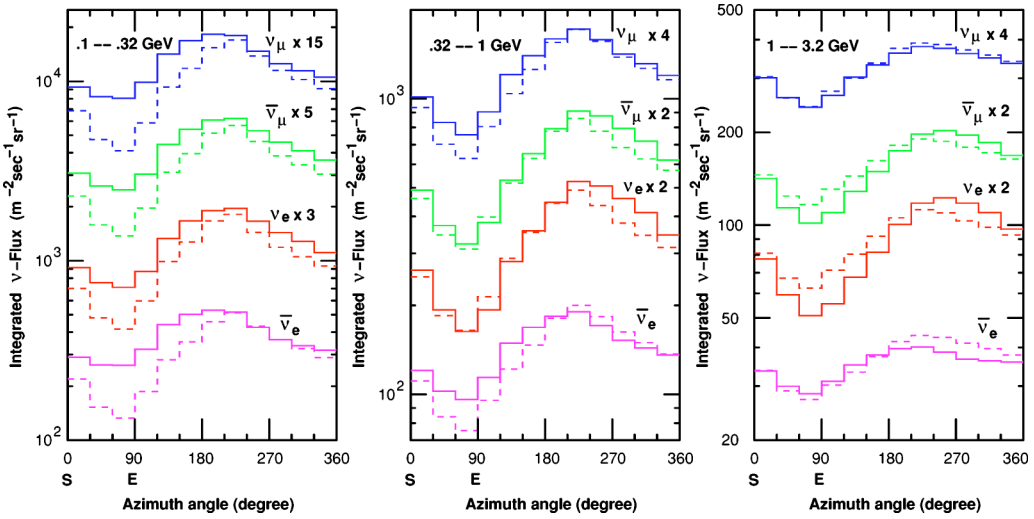

FIG. 13. (Color online) Azimuth angle dependence of the atmospheric neutrino flux at Kamioka, averaged over the zenith angle range $-0.5<\cos\theta<0.5$. The solid lines show the 3D result and the dashed lines the 1D result.

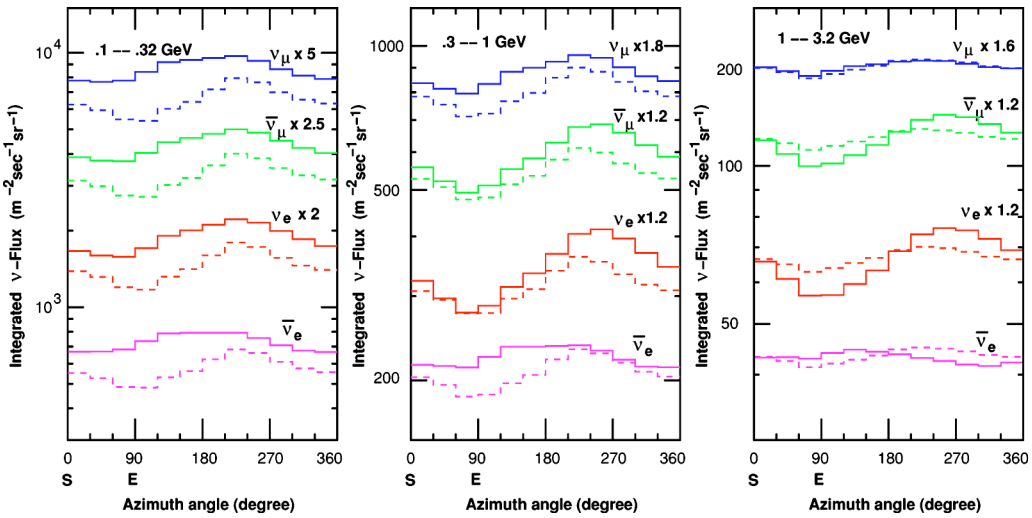

FIG. 14. (Color online) Azimuth angle dependence of the atmospheric neutrino flux at North America, averaged over the zenith angle range $-0.5<\cos\theta<0.5$. The solid lines show the 3D result and the dashed lines the 1D result.

ence between the neutrino fluxes calculated by three-dimensional and one-dimensional schemes are very small at the target energies here, we include the one-dimensional calculations from Refs. [7] (HKKM95) and [8] (BARTOL) in this comparison, and plot them in Fig. 15. Note that, as the 1D results are almost the same as the 3D case in this energy region, and are identical above 100 GeV, they are referred just as this work in this section. Since the energy region available in the DIPOLE case is limited to below 10 GeV, it is omitted from the comparisons.

The larger fluxes in HKKM95 and BARTOL are due to the larger primary flux model used in HKKM95 (Fig. 1) and by the harder secondary spectrum in the hadronic interaction model (TARGET-I) used in BARTOL. We note that the ratios $(\nu_\mu+\bar{\nu}_\mu)/(\nu_e+\bar{\nu}_e)$ obtained for different calculations are very close. The agreement among the different calculations is well within 5 % at most energies. However, the ratios $\nu_\mu/\bar{\nu}_\mu$ and $\nu_e/\bar{\nu}_e$ show larger differences. The differences of $\nu_e/\bar{\nu}_e$ and $\nu_\mu/\bar{\nu}_\mu$ above a few GeV are caused by differences in the pion and kaon productions and their charge ratios in interactions above a few tens of GeV. In particular, $\nu_e/\bar{\nu}_e$ and $\nu_\mu/\bar{\nu}_\mu$ above 100 GeV are related to the kaon production in the hadronic interaction at energies above 1 TeV. Note it is still difficult to examine the hadronic interaction model at these energies.

TABLE IV. Max/Min ratio in Figs. 13 and 14 as the amplitude of the azimuthal angle variation.

E_ν(GeV)	ν_μ	$\bar{\nu}_\mu$	ν_e	$\bar{\nu}_e$	ν_μ	$\bar{\nu}_\mu$	ν_e	$\bar{\nu}_e$
	Kamioka, 3D				Kamioka, 1D			
0.1–.32	2.27	2.51	2.75	2.03	4.13	4.13	4.36	3.85
.32–1.0	2.27	2.82	3.22	1.98	2.73	2.76	2.98	2.65
1.0–3.2	1.58	2.00	2.42	1.42	1.61	1.63	1.80	1.61
	North America, 3D				North America, 1D			
0.1–.32	1.26	1.33	1.40	1.19	1.47	1.48	1.54	1.41
.32–1.0	1.20	1.39	1.49	1.11	1.27	1.28	1.31	1.26
1.0–3.2	1.07	1.25	1.35	1.07	1.08	1.09	1.12	1.09

Next, we study the zenith angle variation of the atmospheric neutrino flux at energies $\gtrsim 10$ GeV with the quantity defined by

$$I_n(\cos\theta)=\int_{E1}^{E2} E_\nu^n \frac{dN_\nu}{dE_\nu}(\cos\theta)dE_\nu. \qquad (2)$$

The neutrino interaction cross section increases approximately in proportion to the neutrino energy. Therefore, $I_1(\cos\theta)$ is approximately proportional to the rate of neutrino events categorized as vertex contained and stop-muon events. High-energy muon neutrinos are also observed, arising from muons produced in the rock. In this case, the neutrino observation probability is proportional to the multiple of [*muon range*]×[*neutrino cross section*]. The muon range is approximately proportional to the muon energy below several 100 GeV, where the energy loss is dominated by ionization. The event rate is approximately proportional to $I_2(\cos\theta)$. Above ~500 GeV, the muon energy loss is dominated by radiative processes [61], and the relation fails.

$I_1(\cos\theta)$ is calculated with $E_1=3.2$ GeV and $E_2=1000$ GeV, and is shown in the left panel of Fig. 16 for this work, HKKM95, BARTOL, and FLUKA. Note, the median energy is ~6 GeV in this integration over all the fluxes. We also depicted the normalized ratio of each flux to this work in the right panel of Fig. 16. As the atmospheric neutrino flux is expected to be symmetric above and below $\cos\theta=0$, we depicted the lower half ($\cos\theta<0$) only. Although there are large differences among theses calculations in the absolute values, the differences of normalized fluxes are small, particularly for ν_μ and $\bar{\nu}_\mu$ ($\lesssim 3$ %).

In Fig. 17, we show the zenith angle variation of I_2 with

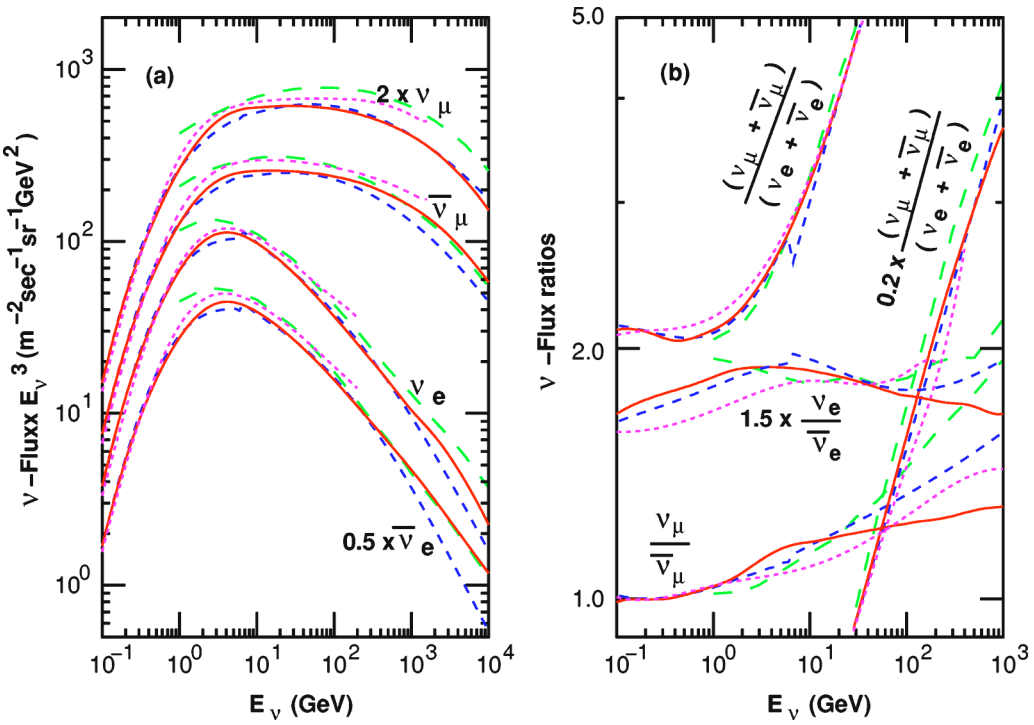

FIG. 15. (Color online) (a) Atmospheric neutrino fluxes averaged over all directions. (b) Flux ratios $(\nu_\mu+\bar{\nu}_\mu)/(\nu_e+\bar{\nu}_e)$, $\nu_\mu/\bar{\nu}_\mu$, and $\nu_e/\bar{\nu}_e$. Solid lines are for this work, dotted lines for HKKM95, dashed lines for FLUKA, and long dashed lines for BARTOL.

$E_1=10$ GeV and $E_2=1000$ GeV for this work, HKKM95, BARTOL, and FLUKA for ν_μ and $\bar{\nu}_\mu$ fluxes. The median energy is ~100 GeV. We find a large difference in absolute values as is expected from the left panel of Fig. 15. However, the differences are small when they are normalized. The ratio of the normalized weighted integral I_2 is shown as a function of zenith angle in the right panel of Fig. 15. The differences in normalized fluxes are $\lesssim 3$ %.

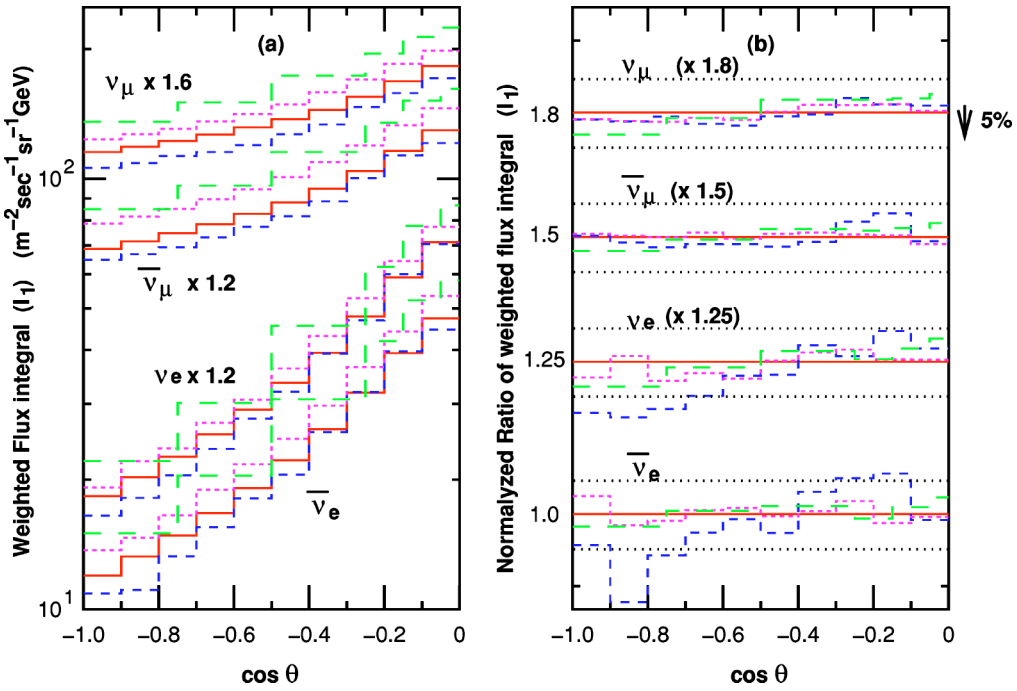

FIG. 16. (Color online) (a) Zenith angle variation of I_1 defined by Eq. (2). (b) The normalized ratio of I_1 of each flux to this work as a function of zenith angle. The solid lines are for this work, dotted lines for HKKM95, dashed lines for FLUKA, and long dashed lines for BARTOL in both panels.

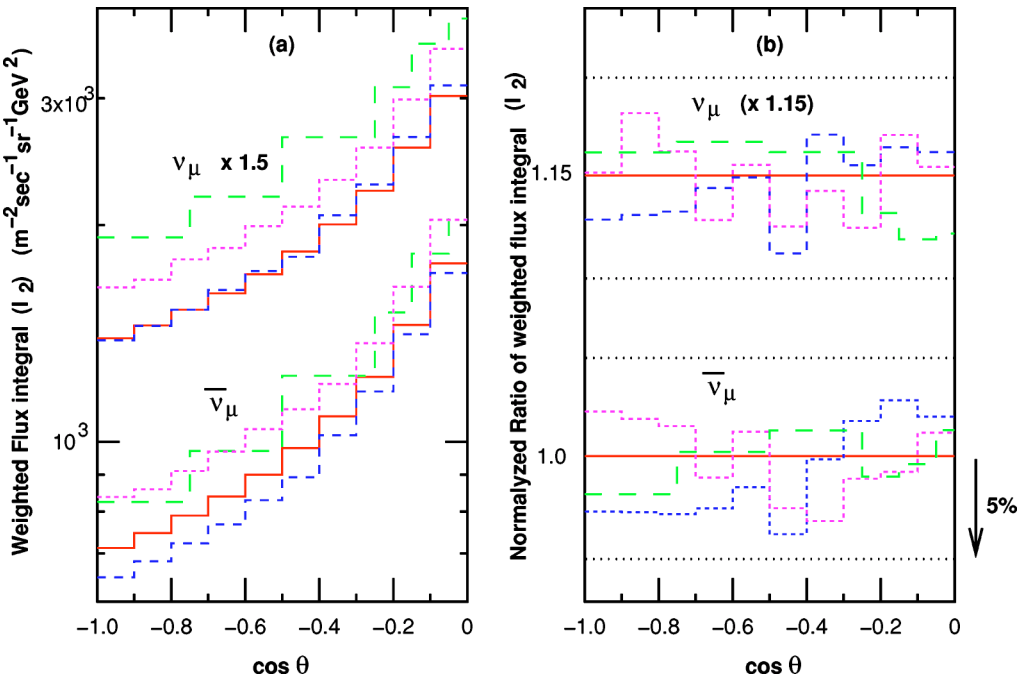

FIG. 17. (Color online) (a) Zenith angle variation of I_2 defined by Eq. (16). (b) Normalized ratio of I_2 of each flux to this work as a function of zenith angle. The solid line is for this work, dotted line for HKKM95, dashed line for FLUKA, and long dashed line for BARTOL in both panels.

As is seen in the left panel of Fig. 15, the ratios $\nu_\mu/\bar{\nu}_\mu$ and $\nu_e/\bar{\nu}_e$ differ significantly between the calculations above 10 GeV. This is due to differences in the pion and kaon productions in the interaction model used by the different calculations. For example the multiplicity for kaons in DPMJET-III is almost 20 % larger than that of FLUKA 97 at 1 TeV. Note, the interaction model used in FLUKA is developed by the authors of FLUKA 97. Despite these differences in the interaction models, the zenith angle dependences of atmospheric neutrinos show good agreement between the different calculations.

VII. PRODUCTION HEIGHT OF ATMOSPHERIC NEUTRINOS

In the analysis of neutrino oscillations, the distance from the point at which the neutrino originates to the detector plays an essential role in determining Δm^2_{23}. To estimate the distance, the arrival zenith angle is used. However, the arrival zenith angle does not determine the distance uniquely, but gives a probability distribution for the distance. In this section, we study the neutrino production height distribution for a given zenith angle. As we assumed the surface of the Earth is a sphere, the distance and production height are related by the formula

$$d=\sqrt{(h^2+2R_e h)+(R_e\cos\theta)^2}-R_e\cos\theta, \qquad (3)$$

where h is the height, R_e is the radius of the Earth, and d is the distance. Note, the production height distribution changes its shape slowly as the zenith angle varies, while the distance distribution changes its shape very quickly near horizontal directions. Therefore, the study of production height distribution is more robust than the direct study of the distance distribution.

In the experimental analysis, the neutrino events are generally grouped in zenith angle bins irrespective of their azimuthal directions. Also, it is difficult to distinguish ν from $\bar{\nu}$ in current experiments. Therefore, we study the production height averaged over the azimuthal angles and for the sum of ν_μ and $\bar{\nu}_\mu$, and ν_e and $\bar{\nu}_e$.

We show the neutrino production height distribution for vertical directions (Fig. 18) and for horizontal directions (Fig. 19). In the figures, we depict the lines for accumulated probabilities of 1, 5, 20, 50, 80, 95, and 99 % for various neutrino energies. Note we study the neutrino production height distribution in steps of $\Delta\cos\theta=0.05$ for a better zenith angle resolution.

For the vertical directions, the production height in the 3D case is higher than that of 1D. However, the differences are small and disappear at $\sim$1 GeV for the median of the production height distribution. Note the difference at the lower tail (1 % line) exists even at a few tens of GeV due to the muon curvature. On the other hand, for the horizontal directions the 3D production height is lower than that of 1D. The differences are larger than those for vertical directions, and are $\sim$10 % for the median of the height distribution even at 1 GeV. However, they agree with each other at several GeV and above.

The differences of the production height resulting from differences in magnetic latitude are small. The neutrino production heights for low energy primary cosmic rays are gen-

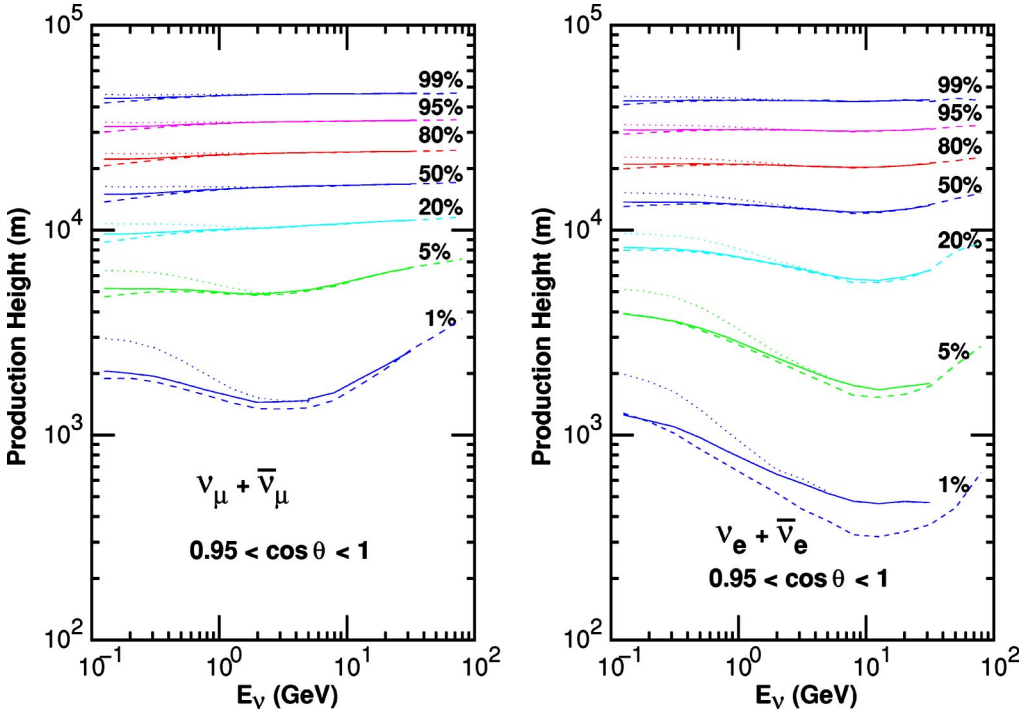

FIG. 18. (Color online) The neutrino production height at near-vertical directions for ν_μ and $\bar{\nu}_\mu$ (left) and ν_e and $\bar{\nu}_e$ (right). The fixed accumulated probabilities of 1, 5, 20, 50, 80, 95, and 99 % for the production height are shown as a function of the neutrino energy. The solid lines are for 3D at Kamioka, dashed lines for 1D at Kamioka, and dotted lines for 3D at North America.

erally higher than those of higher energy primary cosmic rays. Therefore, the neutrino production height at high magnetic latitude is a little higher than that at low magnetic latitude.

Note, the neutrino production height distribution has an azimuthal variation, mainly due to the muon curvature in the geomagnetic field. The production heights of ν_μ and $\bar{\nu}_e$ coming from eastern directions are lower than those coming from

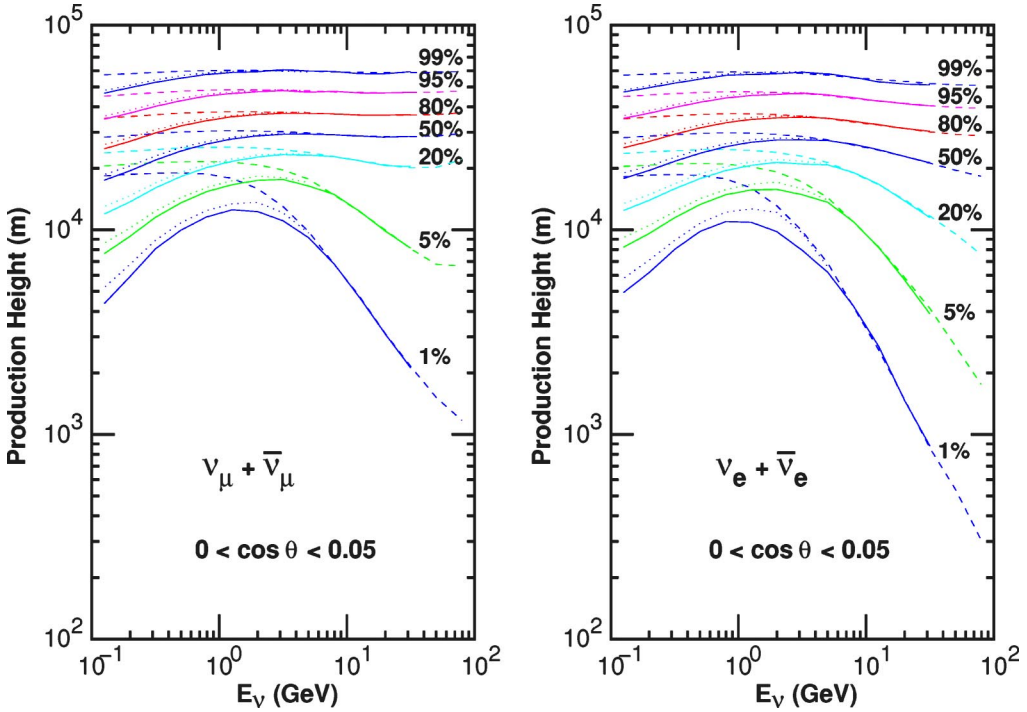

FIG. 19. (Color online) The neutrino production height at near-horizontal directions for $\nu_\mu + \bar{\nu}_\mu$ (left) and $\nu_e + \bar{\nu}_e$ (right). The fixed accumulated probabilities of 1, 5, 20, 50, 80, 95, and 99 % for the production height are shown as a function of the neutrino energy. The solid lines are for 3D at Kamioka, dashed lines for 1D at Kamioka, and dotted lines for 3D at North America.

western directions, and the production heights of $\bar{\nu}_\mu$ and ν_e coming from eastern directions are higher than those coming from western directions. The azimuthal variation of the median production height for the horizontal directions is $\sim \pm 10\,\%$ for ν_e and $\bar{\nu}_e$, and $\sim \pm 5\,\%$ for ν_μ and $\bar{\nu}_\mu$ at a few GeV, and they slowly decrease with the neutrino energy.

The production heights for ν_μ and $\bar{\nu}_\mu$ are a little different even for the vertical direction. Considering the fact that the major component of cosmic rays is protons, a relatively larger number of ν_μ are created by pions rather than muons, and a relatively larger number of $\bar{\nu}_\mu$ are created by muons than pions. The decay products of muons are generally produced at lower altitudes than the decay products of pions. This is also the reason why we see a larger muon curvature effect in $\bar{\nu}_\mu$'s than in ν_μ's. This results in a small difference in the production height for ν_μ and $\bar{\nu}_\mu$. For ν_e and $\bar{\nu}_e$, this mechanism is not relevant, and the production heights are almost the same.

VIII. SUMMARY AND DISCUSSION

We have revised the calculation of the atmospheric neutrino flux, according to recent developments in primary cosmic ray observations and hadronic interaction models. We have also updated the calculations from a one- to a three-dimensional scheme. For the interaction model, we compared the available interaction models with the secondary cosmic rays observed at balloon altitudes, and selected DPMJET-III as the preferred model for this study. We have constructed an inclusive hadronic interaction code based on DPMJET-III for speed. The computation speed is very important in the three-dimensional calculation. We have processed 307 618 204 971 cosmic rays with $E_k/A > 1$ GeV for lower-energy neutrino fluxes, and 415 711 823 606 cosmic rays with $E_k/A > 10$ GeV for neutrino fluxes above 10 GeV. Combining both simulations, the statistical error due to the Monte Carlo method is negligibly small for neutrino energies below a few tens of GeV.

With the primary fluxes accurately determined by BESS and AMS below 100 GeV, the DPMJET-III interaction model, and the fast three-dimensional simulation code for the cosmic ray propagation, we consider we have reduced the uncertainty to $\sim 10\,\%$ in the calculation of the atmospheric neutrino flux at energies below 10 GeV, since we could reproduce the muon fluxes at various altitude with good accuracy from 1 to a few 10 GeV [52,53] in this calculation scheme. However, for the atmospheric neutrino flux above 10 GeV, the uncertainties in the atmospheric neutrino fluxes are still large due to the uncertainties of the primary cosmic ray flux and interaction model above 100 GeV.

The differences we find between the one- and three-dimensional calculation schemes are similar to those we found in the previous study with a dipole geomagnetic field. When we average the atmospheric neutrino flux over azimuthal angles, the fluxes calculated in the three-dimensional scheme quickly converge with those calculated in the one-dimensional scheme at a few GeV. With the larger statistics, however, it becomes clear that muon curvature affects the horizontal neutrino flux even at energies $\gtrsim 10$ GeV, while most other ''three-dimensional effects'' disappear at a few GeV.

In comparison with other calculations of atmospheric neutrino flux, we find the zenith angle dependences of different calculations are very similar, although there are differences in the absolute values. The remaining differences of the zenith angle dependence at higher energies ($\gtrsim 10$ GeV) are consistent with the uncertainty of kaon production in the hadronic interaction [62]. Therefore, we may conclude that the main reason for the remaining difference of the zenith angle dependence is in the kaon production of hadronic interaction model used by different calculations. Note, there are large differences in the interaction model used by the different calculations, as is known from the large $\nu_e/\bar{\nu}_e$ and $\nu_\mu/\bar{\nu}_m u$ differences at higher energies.

The production height distributions in the one- and three-dimensional calculation schemes are different depending on the arrival direction. When they are averaged over azimuthal directions, they agree with each other well above a few GeV, except for a small distortion at the lower tail for the vertical directions. This situation is similar to that of the flux value. There are azimuthal variations of the production height due to the muon curvature, however, it is difficult to study them in detail with the statistics of this work. For the experimental study of atmospheric neutrinos for neutrino oscillations, the azimuthal variations are not important.

It is interesting that the effect of albedo particles observed by AMS at satellite altitudes is seen in the neutrino production time distribution. The contribution of such particles to the atmospheric neutrino flux is a little higher for the low magnetic latitude site (Kamioka) than the high magnetic latitude site (North America), but small ($\ll 1\,\%$) for both sites.

We expect that the validity of the calculation scheme and the effect of the muon curvature will be confirmed by the observation of the azimuthal variation of the neutrino events. Although the statistics are still insufficient, the SuperKamiokande experiment observed a larger amplitude of the azimuthal variation for the e-like events than that for the μ-like events [63,64] as is predicted in Sec. V B. We would like to note that the muon curvature effect has been confirmed by the azimuthal variation of the muon flux with an amplitude almost the same as the value predicted in our calculation scheme [65].

ACKNOWLEDGMENTS

We are grateful to J. Nishimura, A. Okada, P. Lipari, T. Sanuki, K. Abe, S. Haino, Y. Shikaze, and S. Orito for useful discussions and comments. We thank P. G. Edwards for the discussions. We also thank ICRR, the University of Tokyo, for the support. This study was supported by Grants-in-Aid, KAKENHI(12047206), from the Ministry of Education, Culture, Sport, Science and Technology (MEXT).

[1] Super-Kamiokande Collaboration, Y. Fukuda *et al.*, Phys. Rev. Lett. **81**, 1562 (1998).

[2] Kamiokande Collaboration, K.S. Hirata *et al.*, Phys. Lett. B **205**, 416 (1988); **280**, 146 (1992); Y. Fukuda *et al.*, *ibid.* **335**, 237 (1994).

[3] IMB Collaboration, D. Casper *et al.*, Phys. Rev. Lett. **66**, 2561 (1991); R. Bechker-Szendy *et al.*, Phys. Rev. D **46**, 3720 (1992).

[4] Soudan2 Collaboration, W.W.M. Allison *et al.*, Phys. Lett. B **446**, 1562 (1999); M. Sanchez *et al.*, Phys. Rev. D **68**, 113004 (2003).

[5] MACRO Collaboration, M. Ambrosio *et al.*, Phys. Lett. B **434**, 451 (1998); **478**, 5 (2000); **566**, 35 (2003).

[6] T. Kajita and Y. Totsuka, Rev. Mod. Phys. **73**, 85 (2001).

[7] M. Honda, T. Kajita, K. Kahahara, and S. Midorikawa, Phys. Rev. D **52**, 4985 (1995).

[8] V. Agrawal, T.K. Gaisser, P. Lipari, and T. Stanev, Phys. Rev. D **53**, 1314 (1996).

[9] G. Battistoni *et al.*, Astropart. Phys. **12**, 315 (2000); *Proceedings of the 28th International Cosmic Ray Conference*, Vol. 3 (Universal Academy Press, Tsukuba, 2003), p. 1399. See also http://www.mi.infn.it/~battist/neutrino.html.

[10] R. Engel, T.K. Gaisser, P. Lipari, and T. Stanev, *Proceedings of the 27th International Cosmic Ray Conference*, Vol. 4 (Copernicus Gessellschaft, Hamburg, 2001), p. 1381.

[11] M. Honda, T. Kajita, K. Kasahara, and S. Midorikawa, *Proceedings of the 27th International Cosmic Ray Conference*, Vol. 3 (Copernicus Gessellschaft, Hamburg, 2001), p. 1162.

[12] M. Honda, T. Kajita, K. Kasahara, and S. Midorikawa, *Proceedings of the 28th International Cosmic Ray Conference*, Vol. 3 (Universal Academy Press, Tsukuba, 2003), p. 1514.

[13] T.K. Gaisser and M. Honda, Annu. Rev. Nucl. Part. Sci. **52**, 153 (2002).

[14] AMS Collaboration, J. Alcaraz *et al.*, Phys. Lett. B **490**, 27 (2000).

[15] BESS Collaboration, T. Sanuki *et al.*, Astrophys. J. **545**, 1135 (2000).

[16] H. Pi *et al.*, Comput. Phys. Commun. **71**, 173 (1992).

[17] A. Ferrari and P.R. Sala, Trieste, ATLAS internal note ATL-PHYS-97-113 Z1997; *Proceedings Workshop on Nuclear Reaction Data and Nuclear Reactors Physics, Design and Safety*, ICTP, Miramare-Trieste, Italy, 1996, edited by A. Gandini and G. Reffo (World Scientific, Singapore, 1998), Vol. 2, p. 424.

[18] S. Roesler, R. Engel, and J. Ranft, *Proceedings of the 27th International Cosmic Ray Conference*, Vol. 1 (Copernicus Gessellschaft, Hamburg, 2001), p. 439; Phys. Rev. D **57**, 2889 (1998).

[19] P. Lipari, Astropart. Phys. **14**, 171 (2000).

[20] P. Lipari, Astropart. Phys. **14**, 153 (2000).

[21] M. Honda, T. Kajita, K. Kasahara, and S. Midorikawa, Phys. Rev. D **64**, 053011 (2001).

[22] J. Wentz, Phys. Rev. D **67**, 073020 (2003); *Proceedings of the 28th International Cosmic Ray Conference*, Vol. 3 (Universal Academy Press, Tsukuba, 2003), p. 1403.

[23] Y. Liu, L. Derome, and M. Buérd, Phys. Rev. D **67**, 073022 (2003); *Proceedings of the 28th International Cosmic Ray Conference*, Vol. 3 (Universal Academy Press, Tsukuba, 2003), p. 1407.

[24] G. Barr *et al.*, *Proceedings of the 28th International Cosmic Ray Conference*, Vol. 3 (Universal Academy Press, Tsukuba, 2003), p. 1411.

[25] T.K. Gaisser *et al.*, *Proceedings of the 27th International Cosmic Ray Conference*, Vol. 5 (Copernicus Gessellschaft, Hamburg, 2001), p. 1643.

[26] W.R. Webber *et al.*, *Proceedings of the 20th International Cosmic Ray Conference*, Vol. 1 (Moscow Nauka, Moscow, 1987), p. 325.

[27] MASS Collaboration, P. Pappini *et al.*, *Proceedings of the 23rd International Cosmic Ray Conference*, Vol. 1 (University of Calgary, Calgary, 1993), p. 579.

[28] LEAP Collaboration, W.S. Seo *et al.*, Astrophys. J. **378**, 763 (1987).

[29] IMAX Collaboration, W. Menn *et al.*, Astrophys. J. **533**, 281 (2000).

[30] CAPRICE Collaboration, G. Boezio *et al.*, Astrophys. J. **518**, 457 (1999).

[31] CAPRICE Collaboration, G. Boezio *et al.*, Astropart. Phys. **19**, 583 (2003).

[32] BESS Collaboration, S. Haino *et al.*, astro-ph/0403704.

[33] M. Ryan, J.F. Ormes, and V.K. Balasubrahmanyan, Phys. Rev. Lett. **28**, 985 (1972).

[34] JACEE Collaboration, K. Asakimori *et al.*, Astrophys. J. **502**, 278 (1998).

[35] I.P. Ivanenko *et al.*, *Proceedings of the 23rd International Cosmic Ray Conference*, Vol. 2 (University of Calgary, Calgary, 1993), p. 17.

[36] RUNJOB Collaboration, A. V. Apanasenko *et al.*, Astropart. Phys. **16**, 13 (2001).

[37] T. Shibata (private communication).

[38] Y. Kawamura *et al.*, Phys. Rev. D **40**, 729 (1989).

[39] J. Engel, T.K. Gaisser, T. Stanev, and P. Lipari, Phys. Rev. D **46**, 5013 (1992).

[40] R. Glauber, in *Lectures in Theoretical Physics*, edited by A.O. Barut and W.E. Brittin (Interscience, New York, 1959); R.J. Glauber and G. Matthiae, Nucl. Phys. **B21**, 135 (1970).

[41] K. Hänssget and J. Ranft, Comput. Phys. **39**, 37 (1986).

[42] B. Nilsson-Almqvist *et al.*, Comput. Phys. Commun. **43**, 387 (1987).

[43] K. Kasahara, *Proceedings of the 24th International Cosmic Ray Conference*, Vol. 1 (Finit di stampare nel luglio, Rome, 1995), p. 399. See also http://eweb.b6.kanagawa-u.ac.jp/~kasahara/ResearchHome/cosmosHome/.

[44] MASS Collaboration, R. Bellotti *et al.*, Phys. Rev. D **53**, 35 (1996).

[45] MASS Collaboration, R. Bellotti *et al.*, Phys. Rev. D **60**, 052002 (1999).

[46] CAPRICE Collaboration, M. Boezio *et al.*, Phys. Rev. Lett. **82**, 4757 (1999).

[47] CAPRICE Collaboration, M. Boezio *et al.*, Phys. Rev. D **62**, 032007 (2000).

[48] BESS Collaboration, T. Sanuki *et al.*, *Proceedings of the 27th International Cosmic Ray Conference*, Vol. 3 (Copernicus Gessellschaft, Hamburg, 2001), p. 950.

[49] BESS Collaboration, Y. Yamamoto *et al.*, *Proceedings of the 28th International Cosmic Ray Conference*, Vol. 3 (Universal Academy Press, Tsukuba, 2003), p. 1167.
[50] BESS Collaboration, K. Abe *et al.*, Phys. Lett. B **564**, 8 (2003).
[51] K. Kasahara *et al.*, Phys. Rev. D **66**, 052004 (2002).
[52] K. Abe *et al.*, *Proceedings of the 28th International Cosmic Ray Conference*, Vol. 3 (Universal Academy Press, Tsukuba, 2003) p.1463.
[53] T. Sanuki *et al.* (unpublished).
[54] BESS Collaboration, M. Motoki *et al.*, Astropart. Phys. **19**, 113 (2003).
[55] BESS Collaboration, T. Sanuki *et al.*, Phys. Lett. B **541**, 234 (2002).
[56] BESS Collaboration, K. Tanizaki *et al.*, *Proceedings of the 28th International Cosmic Ray Conference*, Vol. 3 (Universal Academy Press, Tsukuba, 2003), p. 1167.
[57] http://nssdc.gsfc.nasa.gov/space/model/models/igrf.html
[58] U.S. Standard Atmosphere, 1976, U.S. Government Printing Office, Washington, D.C., 1976. See also http://nssdc.gsfc.nasa.gov/space/model/atmos/us_standard.html.
[59] For example, J.M. Picone *et al.*, J. Geophys. Res. **107**(A12), 1468 (2002); See also http://nssdc.gsfc.nasa.gov/space/model/atmos/nrlmsise00.html.
[60] M. Honda *et al.*, Neutrino 2002 poster paper (unpublished). See also http://www.icrr.u-tokyo.ac.jp/~mhonda.
[61] S.R. Kel'ner and Yu.D. Kotov, Sov. J. Nucl. Phys. **7**, 237 (1968); B.P. Kokoulin and A.A. Petrukhin, *Proceedings of the 11th International Cosmic Ray Conference*, Vol. 29, Suppl. 4 (Central Research for Physics, Budapest, 1969), p. 277.
[62] M. Honda, *Proceedings Noon 2003* (World Scientific, Kanazawa). See also http://www.icrr.u-tokyo.ac.jp/~mhonda.
[63] Super-Kamiokande Collaboration, T. Futagami *et al.*, Phys. Rev. Lett. **82**, 5194 (1999).
[64] S. Moriyama *et al.*, *Proceedings of the 28th International Cosmic Ray Conference*, Vol. 3 (Tsukuba, Ibaraki, Japan, 2003), p. 1263.
[65] P.N. Diep *et al.* (unpublished).